Xiaokun Ma
Mechatronics Research Laboratory,
Department of Mechanical and
Nuclear Engineering,
The Pennsylvania State University,
University Park, PA 16802
e-mail: xma-me@psu.edu

Andrew Wilson
Mechatronics Research Laboratory,
Department of Mechanical and
Nuclear Engineering,
The Pennsylvania State University,
University Park, PA 16802
e-mail: ajw5360@psu.edu

Christopher D. Rahn[1]
Professor
Mechatronics Research Laboratory,
Department of Mechanical and
Nuclear Engineering,
The Pennsylvania State University,
University Park, PA 16802
e-mail: cdrahn@psu.edu

Susan Trolier-McKinstry
Professor
Materials Research Institute,
Department of Materials
Science and Engineering,
The Pennsylvania State University,
University Park, PA 16802
e-mail: stmckinstry@psu.edu

Efficient Energy Harvesting Using Piezoelectric Compliant Mechanisms: Theory and Experiment

Piezoelectric energy harvesters typically perform poorly in the low frequency, low amplitude, and intermittent excitation environment of human movement. In this paper, a piezoelectric compliant mechanism (PCM) energy harvester is designed that consists of a polyvinylidene diflouoride (PVDF) unimorph clamped at the base and attached to a compliant mechanism at the tip. The compliant mechanism has two flexures that amplify the tip displacement to produce large motion of a proof mass and a low frequency first mode with an efficient (nearly quadratic) shape. The compliant mechanism is fabricated as a separate, relatively rigid frame with flexure hinges, simplifying the fabrication process, and surrounding and protecting the piezoelectric unimorph. The bridge structure of the PCM also self-limits the response to large amplitude impacts, improving the device robustness. Experiments show that the compliant hinge stiffness can be carefully tuned to approach the theoretical high power output and mode shape efficiency.
[DOI: 10.1115/1.4032178]

1 Introduction

Wireless electronic devices are widely used in civilian and military applications with batteries providing the requisite power. Batteries have well-known disadvantages in low power devices, especially those used in the human body, such as limited lifetime, environmental pollution, and inconvenient maintenance. Capturing energy from the ambient environment using piezoelectric energy harvesters has the potential to overcome these limitations [1–5]. Body-based energy harvesting using piezoelectric materials has two main barriers: the low frequency and intermittent nature of human movements. Researchers have found that the dominant motion frequencies for common activities, such as running, walking, and relaxing, are mostly below 10 Hz [6,7].

The most common configuration for a piezoelectric energy harvester is the proof mass cantilever design shown in Fig. 1. An experimental prototype of the device is shown in Fig. 2. It is difficult to make the small, low frequency cantilever energy harvesters designed for human movements. In addition, the strain distribution in the first mode decreases from the base to the tip, reducing the efficiency. Maximum power (100% mode shape efficiency) is achieved when the piezoelectric layer is uniformly strained to its limit along the entire length of the beam [8]. Researchers used a lead zirconate titanate (PZT) unimorph with [9,10] or without [11] a tip mass and bimorph cantilever configurations with series and parallel connections of piezoceramic layers that can enhance power output [12–14]. In order to amplify the electrical power output and improve the effective bandwidth of the harvester, researchers used a spring-mass system at the base of a conventional bimorph cantilever beam to increase power output [15].

Researchers also investigated a clamped unimorph piezoelectric plate structure [16,17]. This device, however, has very high natural frequencies and relatively inefficient strain distributions. Devices that up-convert ambient vibration frequency to a higher frequency achieve better electromechanical coupling and efficiency. Buckled slender bridges [18], clamped–clamped spiral beams [19], magnetically actuated piezoelectric beams [20–22], and impact-driven, coupled beams [23,24] have used up-conversion. Frequency up-conversion devices can harvest energy from low frequency excitations, but they can be difficult to build and analyze.

Some researchers focused on improving the strain distribution in the piezoelectric layer to maximize power and energy harvesting efficiency. For example, an initially curved piezoceramic unimorph was designed to generate more charge [25]. Modifying the beam geometry was shown to provide more uniform strain, such as using a trapezoid beam [26]. None of these designs, however, provide 100% mode shape efficiency.

In this paper, we propose a PCM energy harvester that can operate at low frequency without a large proof mass and provide uniform strain for high mode shape efficiency. First, we introduce the PCM design and fabrication process and derive its frequency domain model. Then, the PCM quadratic boundary condition is derived to ensure a highly efficient mode shape. Impedance matching for maximum power determines the optimal load resistance. Finally, experiments are performed to validate the PCM energy harvester model predictions.

2 PCM Design

Figure 3 shows the design and model of the PCM energy harvester. The unimorph beam consists of top and bottom electroded

[1]Corresponding author.

Contributed by the Technical Committee on Vibration and Sound of ASME for publication in the Journal of Vibration and Acoustics. Manuscript received April 29, 2015; final manuscript received November 24, 2015; published online January 20, 2016. Assoc. Editor: Mohammed Daqaq.

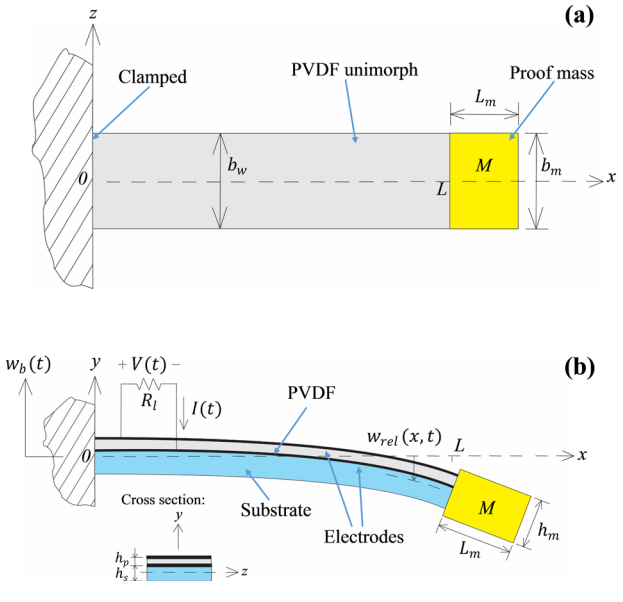

Fig. 1 Proof mass cantilever (*a*) design and (*b*) model

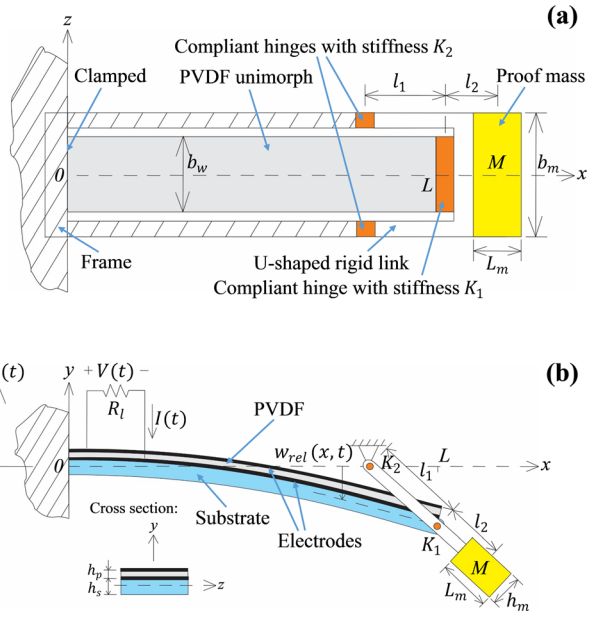

Fig. 3 PCM (*a*) design and (*b*) model

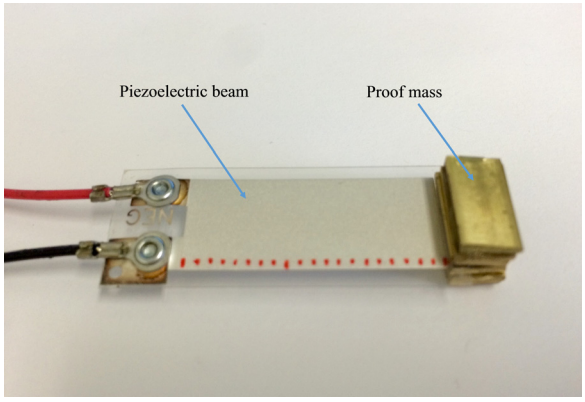

Fig. 2 Photograph of a proof mass cantilever prototype

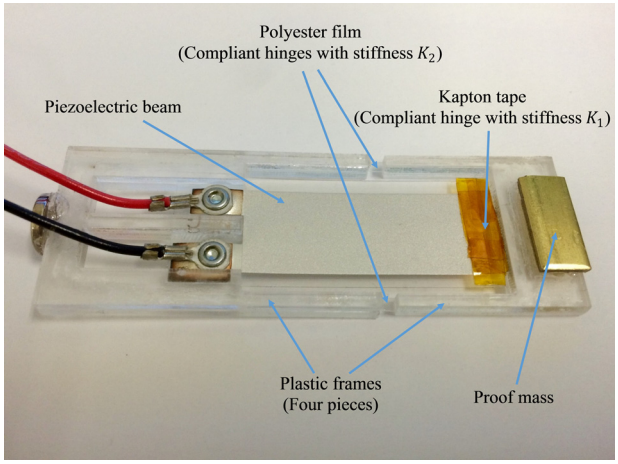

Fig. 4 Photograph of a PCM prototype

PVDF bonded to a substrate layer, the same as in the cantilever in Fig. 1. One end of the beam is clamped to a rigid frame and the other end is connected to the middle of a U-shaped rigid link by a compliant hinge with torsional spring stiffness K_1. The other two compliant hinges, which connect the frame and the U-shaped link, have torsional spring stiffness K_2. We assume the U-shaped link is rigid and massless and the proof mass is attached at the tip of the link. The compliant mechanism at the tip can amplify the tip displacement to produce large motion of the proof mass. The external electrical circuit consists of a resistive load that is electrically in parallel with the internal capacitance of the PVDF layer.

We use a PVDF unimorph from Measurement Specialties, Inc. (LDT1-028 K) to build the PCM device and a frame to simplify the PCM fabrication process. As shown in Fig. 3(*a*) and the experimental prototype in Fig. 4, the PCM energy harvester consists of two parts: the piezoelectric beam and the plastic frame around the beam. The frame has base and tip rigid parts connected by low stiffness hinges. The frame is a sandwich structure of rigid plastic bonded on top and bottom of a flexible plastic film. One end of the piezoelectric beam is glued between two plastic frames to form the clamped boundary condition and provide a reliable connection for the dual wire leads. The other end is connected via a hinge of tunable stiffness (formed from layers of Kapton tape) to the U-shaped link. The thin polyester film between the two plastic frames provides the compliant hinges with stiffness K_2. For the compliant hinge connecting the beam and the U-shaped link, we obtain the required torsional stiffness K_1 by adjusting the number of Kapton tape layers. Finally, the required proof mass can be glued onto the tip of the U-shaped link.

3 PCM Model

The equivalent proof mass

$$M_{\text{eq}} = M\left(\frac{l_1 + l_2}{l_1}\right)^2 + J\left(\frac{1}{l_1}\right)^2 \tag{1}$$

where, as shown in Fig. 3, l_1 is the distance from the frame hinge to the beam tip and l_2 is the distance from the beam tip to the center of the proof mass. The proof mass and rotary inertia are

$$M = \rho_m L_m b_m h_m \tag{2}$$

$$J = \frac{1}{12} M\left(L_m^2 + h_m^2\right) \tag{3}$$

respectively, where ρ_m, L_m, b_m, and h_m are the density, length, width, and thickness of the proof mass, respectively. The transverse deflection of the beam

$$w(x,t) = w_{\text{rel}}(x,t) + w_b(t) \tag{4}$$

where $w_{\text{rel}}(x,t)$ is the transverse deflection of the beam relative to its base, $w_b(t)$ is the base excitation, x is the position along the beam longitudinal axis, and t is the time.

The motion of the beam and proof mass contribute to the kinetic energy

$$\begin{aligned} T =& \frac{1}{2}\int_0^L m\dot{w}(x,t)^2 dx \\ &+ \frac{1}{2}M\left[\dot{w}_b(t) + \frac{l_1+l_2}{l_1}\dot{w}_{\text{rel}}(L,t)\right]^2 \\ &+ \frac{1}{2}J\left[\frac{1}{l_1}\dot{w}_{\text{rel}}(L,t)\right]^2 \end{aligned} \tag{5}$$

where L is the length of the beam and dots and primes indicate partial differentiation with respect to t and x, respectively. For the composite unimorph beam, the mass per unit length

$$m = b_w(\rho_s h_s + \rho_p h_p), \tag{6}$$

where b_w is the beam width, ρ_s, h_s are the substrate density and thickness, respectively, and ρ_p, h_p are the PVDF density and thickness, respectively.

The potential energy V comes from the beam bending stiffness EI and the two compliant hinges with torsional spring stiffness K_1 and K_2

$$\begin{aligned} V =& \frac{1}{2}\int_0^L EIw''_{\text{rel}}(x,t)^2 dx \\ &+ \frac{1}{2}K_1\left[\frac{1}{l_1}w_{\text{rel}}(L,t) - w'_{\text{rel}}(L,t)\right]^2 \\ &+ \frac{1}{2}K_2\left[\frac{1}{l_1}w_{\text{rel}}(L,t)\right]^2 \end{aligned} \tag{7}$$

The PCM bridge structure supports the unimorph and introduces an axial tensioning nonlinearity. In this paper, we focus on the linear response under relatively small base excitation and ignore the nonlinear stretching strain in the potential energy. The stiffness for constant rectangular cross section flexure hinge is

$$K = \frac{E_h b_h h_h^3}{12 L_h} \tag{8}$$

where E_h, b_h, h_h, and L_h are the Young's modulus, width, thickness, and length of the compliant hinge, respectively [27]. The bending stiffness of the composite unimorph beam

$$EI = \frac{1}{3}b_w\left[E_s\left(h_b^3 - h_a^3\right) + E_p\left(h_c^3 - h_b^3\right)\right] \tag{9}$$

where E_s and E_p are the Young's moduli of the substrate and PVDF layers, respectively [11]. The parameters h_a, h_b, and h_c are listed in Table 1 and depend on the thicknesses and Young's moduli of the substrate and PVDF layers.

The virtual work includes the effects of viscous air damping, strain rate damping, and the electrical work of the external circuit on the beam

$$\begin{aligned} \delta W =& -\int_0^L c_a\dot{w}(x,t)\delta w(x,t)dx \\ &- \int_0^L c_s I\dot{w}''_{\text{rel}}(x,t)\delta w''_{\text{rel}}(x,t)dx \\ &+ M_V(t)\delta w'_{\text{rel}}(0,t) - M_V(t)\delta w'_{\text{rel}}(L,t) \end{aligned} \tag{10}$$

where c_a and c_s are the viscous air and strain rate damping coefficients, respectively, and I is the equivalent area moment of inertia. Viscous air damping and strain rate damping are related to the mechanical damping ratio

$$\zeta_r = \frac{c_s I\omega_r}{2EI} + \frac{c_a}{2m\omega_r} \tag{11}$$

where ω_r is the undamped natural frequency of the rth mode [11,28]. The moment term

$$M_V(t) = \vartheta V(t) \tag{12}$$

where $\vartheta = -Ep^* b_w^* h_{pc}^* d_{31}$ and d_{31} is the piezoelectric constant [11].

Hamilton's principle $\delta\int_0^t (T - V + W)dt = 0$ is applied to produce the field equation

$$\begin{aligned} &EIw''''_{\text{rel}}(x,t) + m\ddot{w}_{\text{rel}}(x,t) + c_s I\dot{w}''''_{\text{rel}}(x,t) + c_a\dot{w}_{\text{rel}}(x,t) \\ &\quad = -m\ddot{w}_b(t) - c_a\dot{w}_b(t) \end{aligned} \tag{13}$$

and four boundary conditions

$$w_{\text{rel}}(0,t) = 0 \tag{14}$$

$$w'_{\text{rel}}(0,t) = 0 \tag{15}$$

Table 1 Transformed cross section parameters

Parameter	Description	Expression
n	Ratio of Young's moduli of the substrate and PVDF layers	$\frac{E_s}{E_p}$
h_{pa}	Distance from the top of the PVDF layer to the neutral axis	$\frac{h_p^2 + 2nh_p h_s + nh_s^2}{2(h_p + nh_s)}$
h_{sa}	Distance from the bottom of the substrate layer to the neutral axis	$\frac{h_p^2 + 2h_p h_s + nh_s^2}{2(h_p + nh_s)}$
h_{pc}	Distance from the center of the PVDF layer to the neutral axis	$\frac{nh_s(h_p + h_s)}{2(h_p + nh_s)}$
h_a	Position of the bottom of the substrate layer from the neutral axis	$-h_{sa}$
h_b	Position of the bottom of the PVDF layer from the neutral axis	$h_{pa} - h_p$
h_c	Position of the top of the PVDF layer from the neutral axis	h_{pa}

$$EIw''_{\text{rel}}(L,t) - K_1\left[\frac{1}{l_1}w_{\text{rel}}(L,t) - w'_{\text{rel}}(L,t)\right] + c_sI\dot{w}''_{\text{rel}}(L,t) + M_V(t) = 0 \tag{16}$$

$$EIw'''_{\text{rel}}(L,t) - M\frac{l_1+l_2}{l_1}\left[\ddot{w}_b(t) + \frac{l_1+l_2}{l_1}\ddot{w}_{\text{rel}}(L,t)\right] - J\frac{1}{l_1^2}\ddot{w}_{\text{rel}}(L,t) - K_1\frac{1}{l_1}\left[\frac{1}{l_1}w_{\text{rel}}(L,t) - w'_{\text{rel}}(L,t)\right] - K_2\frac{1}{l_1^2}w_{\text{rel}}(L,t) + c_sI\dot{w}'''_{\text{rel}}(L,t) = 0 \tag{17}$$

From piezoelectric constitutive laws, we obtain the electrical circuit equation with mechanical coupling

$$C_p\dot{V}(t) + \frac{1}{R_l}V(t) = \int_0^L E_pb_wd_{31}\dot{S}_1(x,t)dx. \tag{18}$$

Here, R_l is the load resistance in the external electrical circuit and $C_p = (Lb_w\varepsilon_{33}^S/h_p)$ is the parallel plate capacitance of the PVDF layer, where ε_{33}^S is the permittivity at constant strain. The average bending strain at position x and time t occurs at the center of the PVDF layer

$$S_1(x,t) = -h_{pc}w''_{\text{rel}}(x,t) \tag{19}$$

Substituting Eq. (19) into Eq. (18), we obtain the electrical circuit equation

$$C_p\dot{V}(t) + \frac{1}{R_l}V(t) = -E_pb_wh_{pc}d_{31}\dot{w}'_{\text{rel}}(L,t) \tag{20}$$

To develop a frequency domain model, we take the Laplace transform of Eq. (13), which has a general solution

$$W_{\text{rel}}(x,s) = C_1(s)e^{\beta(s)x} + C_2(s)e^{-\beta(s)x} + C_3(s)e^{j\beta(s)x} + C_4(s)e^{-j\beta(s)x} - W_b(s) \tag{21}$$

where $\beta(s) = \sqrt[4]{-[(ms^2+c_as)/(\text{EI}+c_sIs)]}$. Taking the Laplace transform of Eqs. (14)–(17) and (20) and substituting the general solution in Eq. (21) generate five equations in the five unknowns $C_1(s)$, $C_2(s)$, $C_3(s)$, $C_4(s)$, and $V(s)$. Thus, we can solve for the transcendental transfer functions $[W(x,s)/W_b(s)]$ and $[V(s)/W_b(s)]$.

Using the transcendental transfer function $[W(x,s)/W_b(s)]$, we obtain the transfer function from base acceleration to tip displacement

$$G_{WL}(s) = \frac{W(L,s)}{s^2W_b(s)} \tag{22}$$

The maximum bending strain at position x occurs at the top of the PVDF layer

$$S_{\max}(x,t) = -h_{pa}w''_{\text{rel}}(x,t) \tag{23}$$

so the transfer function from base acceleration to maximum strain is

$$G_S(x,s) = \frac{-h_{pa}W''_{\text{rel}}(x,s)}{s^2W_b(s)} = \frac{-h_{pa}W''(x,s)}{s^2W_b(s)} \tag{24}$$

Similarly, using the transcendental transfer function $[V(s)/W_b(s)]$, we obtain the transfer function from base acceleration to voltage

$$G_V(s) = \frac{V(s)}{s^2W_b(s)} \tag{25}$$

The external circuit is a resistive load R_l, so the amplitude of the power transfer function is

$$|G_P(j\omega)| = \frac{|G_V(j\omega)|^2}{R_l} \tag{26}$$

4 PCM Quadratic Boundary Condition

For high mode shape efficiency, we adjust the flexure stiffness K_1 to maximize the strain distribution uniformity along the length of the beam. Equation (19) shows that the bending strain is proportional to the curvature of the beam, so uniform strain means constant curvature and, for small displacement, a quadratic mode shape. A quadratic mode shape will not satisfy Eq. (13) unless the frequency is zero. We can approach this result if the proof mass is large compared to the unimorph mass so the unimorph bends like a static spring. We can approach a quadratic mode shape under these conditions if the shear force is zero but moment is nonzero at the position $x = L$.

The general solution to the separable eigenvalue problem associated with Eq. (13) is

$$W_{\text{rel}}(x) = C_1e^{bx} + C_2e^{-bx} + C_3e^{jbx} + C_4e^{-jbx} \tag{27}$$

where $b = \sqrt[4]{(m\omega^2/EI)}$. We can solve for the unknowns C_1, C_2, C_3, and C_4 using the clamped boundary condition at $x = 0$ and zero shear force boundary condition at $x = L$ to produce

$$\begin{aligned} W_{\text{rel}}(x) = {} & C_5[e^{(1+2j)Lb} + je^{Lb} + (1+j)e^{jLb}]e^{bx} \\ & + C_5[e^{Lb} + je^{(1+2j)Lb} + (1+j)e^{(2+j)Lb}]e^{-bx} \\ & - C_5[e^{jLb} + je^{(2+j)Lb} + (1+j)e^{Lb}]e^{jbx} \\ & - C_5[e^{(2+j)Lb} + je^{jLb} + (1+j)e^{(1+2j)Lb}]e^{-jbx} \end{aligned} \tag{28}$$

where C_5 is an arbitrary scale factor.

Taking the Laplace transform of Eqs. (16) and (17), substituting $s = j\omega$, and neglecting the moment term $M_V(t)$, we obtain

$$EIW''_{\text{rel}}(L) - K_1\left[\frac{1}{l_1}W_{\text{rel}}(L) - W'_{\text{rel}}(L)\right] + jc_sI\omega W''_{\text{rel}}(L) = 0 \tag{29}$$

$$M_{\text{eq}}\omega^2W_{\text{rel}}(L) - K_1\frac{1}{l_1}\left[\frac{1}{l_1}W_{\text{rel}}(L) - W'_{\text{rel}}(L)\right] - K_2\frac{1}{l_1^2}W_{\text{rel}}(L) + jc_sI\omega W'''_{\text{rel}}(L) = 0 \tag{30}$$

Substituting Eq. (28) into Eqs. (29) and (30), we find the quadratic boundary condition

$$K_1 = \frac{\sqrt{2}l_1b^2\sqrt{(c_sI\omega)^2 + EI^2}|\sigma_1|}{|(1+j)\sigma_2 - 2l_1b\left(j + e^{2Lb} - e^{2jLb} - je^{2(1+j)Lb}\right)|} \tag{31}$$

$$M_{\text{eq}} = \frac{\left|\sqrt{2}l_1b^2\sqrt{(c_sI\omega)^2 + EI^2}|\sigma_1| + (1+j)K_2\sigma_2\right|}{\sqrt{2}\omega^2l_1^2|\sigma_2|} \tag{32}$$

where

$$\sigma_1 = (e^{Lb} + e^{jLb})^2 + \left(1 + e^{(1+j)Lb}\right)^2$$

$$\sigma_2 = (e^{Lb} + e^{jLb})^2 - \left(1 + e^{(1+j)Lb}\right)^2$$

The ideal value of K_2 is zero and M_{eq} can be simplified based on this assumption. However, the compliant hinges connecting the frame and U-shaped link cannot be built to have zero torsional spring stiffness and we need to find the value of K_2 via experiment

to determine M_{eq}. Given the PCM parameters and vibration frequency ω, we can calculate the spring stiffness K_1 and equivalent proof mass M_{eq} that result in a nearly quadratic mode shape.

5 Maximum Power Analysis

If the maximum strain in the PVDF reaches its limit S_{lim}, the energy harvester has maximum power P_{max}. However, the theoretical maximum power $P_{max,theory}$ is obtained when the entire volume of the PVDF is sinusoidally strained to its limit S_{lim} at a given frequency ω. We define the mode shape efficiency

$$\eta = \frac{P_{max}}{P_{max,theory}} \tag{33}$$

To calculate the theoretical maximum power, we start with the electrical circuit equation given by Eq. (18) and assume that the entire volume of the PVDF is sinusoidally strained to its limit S_{lim} at a given frequency ω. $S_1(x,t)$ is no longer a function of position x and Eq. (18) becomes

$$\frac{Lb_w\varepsilon_{33}^S}{h_p}\dot{V}(t) + \frac{1}{R_l}V(t) = E_p L b_w d_{31}\dot{S}_1(t) \tag{34}$$

From Eq. (34), the transfer function from strain input to voltage output is

$$G(s) = \frac{V(s)}{S_1(s)} = \frac{E_p L b_w h_p d_{31} R_l s}{Lb_w\varepsilon_{33}^S R_l s + h_p} \tag{35}$$

To determine the amplitude of voltage response to $S_1(t) = S_{lim}\sin(\omega t)$, we substitute $s = j\omega$ into Eq. (35) and calculate its magnitude

$$V = S_{lim}|G(j\omega)| = \frac{S_{lim}E_p L b_w h_p d_{31} R_l \omega}{\sqrt{\left(Lb_w\varepsilon_{33}^S R_l\omega\right)^2 + h_p^2}} \tag{36}$$

From Eq. (36), we calculate the output power amplitude

$$P = \frac{V^2}{R_l} = \frac{(S_{lim}E_p L b_w h_p d_{31}\omega)^2 R_l}{\left(Lb_w\varepsilon_{33}^S R_l\omega\right)^2 + h_p^2} \tag{37}$$

To determine the theoretical maximum power, we differentiate Eq. (37) with respect to R_l and equate to zero to find the optimal, impedance-matched load resistance

$$R_{opt} = \frac{h_p}{Lb_w\varepsilon_{33}^S\omega} = \frac{1}{C_p\omega} \tag{38}$$

From Eq. (38), we know that the theoretical maximum power is achieved when the resistance in the external electrical circuit is matched to the parallel plate capacitance of the PVDF. Substituting Eq. (38) into Eq. (37), we obtain the amplitude of theoretical maximum power

$$P_{max,theory} = \frac{(S_{lim}E_p d_{31})^2 L b_w h_p \omega}{2\varepsilon_{33}^S} \tag{39}$$

6 Experimental Validation

6.1 Experimental Setup. Figure 5 shows the experimental setup used to measure the frequency responses from base acceleration to tip displacement and voltage. One end of the PCM energy harvester is clamped to the stinger of an electrodynamic shaker. The shaker is placed horizontally and provides a sine sweep excitation from 0 to 20 Hz. A laser vibrometer measures the tip and base displacements of the PCM under the excitation. We also measure the base acceleration using the laser vibrometer. A resistance box is connected in parallel with the piezoelectric layer and adjusted from 10 Ω to 21 MΩ for impedance matching. The displacement signals from the laser vibrometer and voltage drop across the resistor are processed by a LABVIEW data acquisition system, which also performs A/D and D/A conversion, amplification, and FFT analysis.

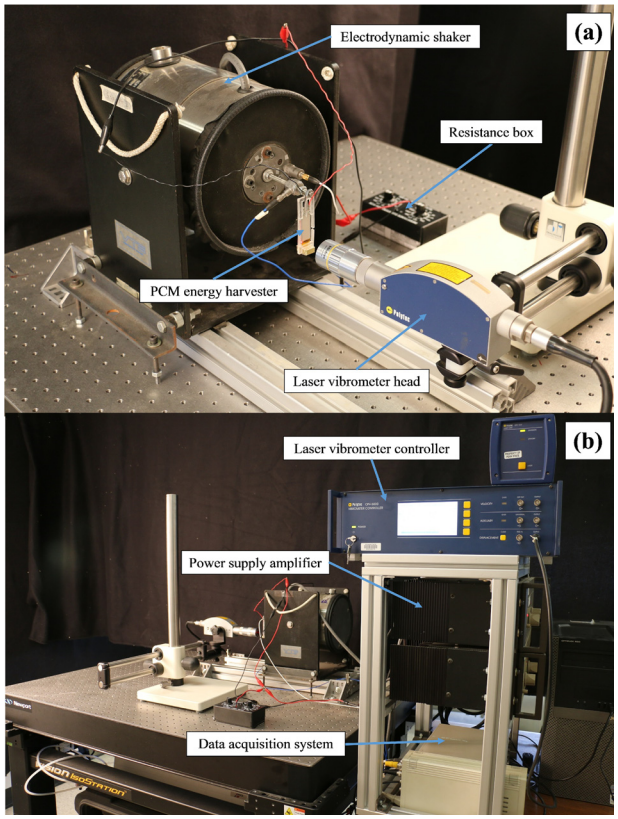

Fig. 5 Experimental setup: (*a*) laser vibrometer and shaker and (*b*) data acquisition system

6.2 Experimental Validation of the PCM Energy Harvester. To provide a baseline for comparison, we analyze the proof mass cantilever and PCM devices side-by-side. Both devices use the same LDT1-028 K laminated PVDF film unimorph from Measurement Specialties, Inc. The PVDF layer is laminated to a sheet of polyester (Mylar) and the dual wire leads attach the harvester to the resistive load. As with the proof mass cantilever design, one end of the PCM is clamped, providing a low stress connection point for the output wires. The material properties of the PVDF unimorph [29] are listed in Table 2. Both devices are designed to have a 5 Hz natural frequency, which is within the bandwidth of human motion. Using Eqs. (38) and (39), we calculate the optimal load resistance and theoretical maximum power at resonance with the same in-plane strain limit in the PVDF. The first mode damping ratio ζ_1 is obtained from experimental modal analysis.

Using Eqs. (22), (25), and (26), we plot the frequency (f) responses of tip displacement, voltage, and power at optimal resistance for both the proof mass cantilever and PCM, shown as blue dashed lines in Fig. 6 and black dashed lines Fig. 7, respectively (see online figures for color). The experimental results for the cantilever are plotted as blue solid lines in Fig. 6 and they match very well with the theory. The optimal stiffness for the compliant hinge K_1 of the PCM is achieved by adjusting Kapton tape thickness to maximize the output power at the first resonance. Figure 7(*a*) shows the tip displacement frequency response for

Table 2 Model parameters

Parameter	Description	Proof mass cantilever	PCM	Units
L	Beam length	30		mm
b_w	Beam width	12.2		mm
h_s	Substrate (Mylar) thickness	125		μm
h_p	PVDF thickness	28		μm
ρ_s	Substrate (Mylar) density	1390		kg/m^3
ρ_p	PVDF density	1780		kg/m^3
ρ_m	Proof mass (brass) density	8600		kg/m^3
E_s	Substrate (Mylar) Young's modulus	5		GPa
E_p	PVDF Young's modulus	3		GPa
d_{31}	Piezoelectric constant	23		pm/V
ε_{33}^S	Permittivity at constant strain	106		pF/m
σ_y	PVDF yield strength	55		MPa
L_m	Proof mass length	6.35	6.35	mm
b_m	Proof mass width	12	12.5	mm
h_m	Proof mass thickness	9	9	mm
ζ_1	First mode damping ratio	2.37%	3.26%	
l_1	PCM base link length		15	mm
l_2	PCM proof mass link length		8	mm
K_1	PCM beam tip hinge torsional spring stiffness		0.243	N·m/rad
K_2	PCM frame hinge torsional spring stiffness		0.0045	N·m/rad

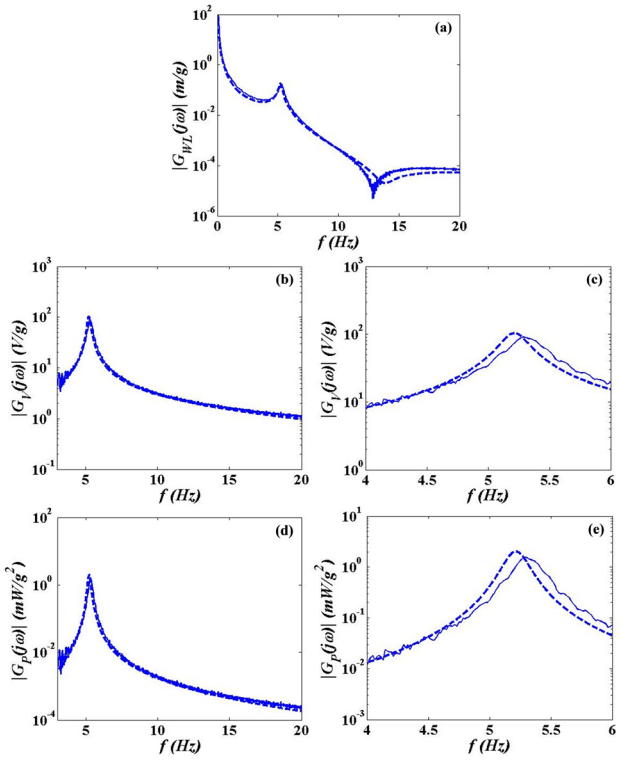

Fig. 6 Proof mass cantilever frequency responses from theory (blue dashed line) and experiment (blue solid line): (*a*) tip displacement, (*b*) voltage, (*c*) enlarged view of voltage, (*d*) power, and (*e*) enlarged view of power (see online figure for color)

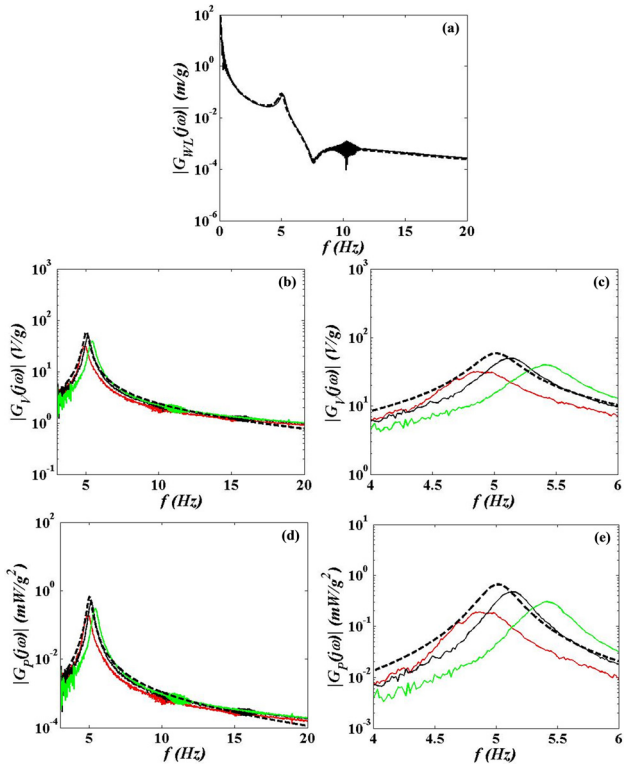

Fig. 7 PCM frequency responses from theory (black dashed line) and experiment (optimal stiffness: black solid line, lower stiffness: red solid line, and higher stiffness: green solid line): (*a*) tip displacement, (*b*) voltage, (*c*) enlarged view of voltage, (*d*) power, and (*e*) enlarged view of power (see online figure for color)

optimal stiffness. The first mode peak around 5 Hz is clearly visible and the experiment matches very well with the model except for some noise around 10 Hz. The tip displacement sensitivity d_{sen} in Table 3 can be read from the resonance peak in Fig. 7(*a*). As can be seen in Figs. 7(*b*) and 7(*d*), the voltage and power frequency responses also match well with the model. Figures 7(*c*) and 7(*e*) provide enlarged views of the voltage and power frequency responses between 4 Hz and 6 Hz. Lower stiffness (red solid lines) and higher stiffness (green solid lines) for the compliant hinge K_1 produce less power than the optimal stiffness (black solid lines; see online figure for color). If Kapton tape is removed from optimal stiffness flexure, the compliant hinge stiffness K_1 and resonance frequency decrease. The compliant hinge stiffness K_1 and resonance frequency increase with the addition of Kapton tape layers. From Figs. 7(*c*) and 7(*e*), we determine the voltage sensitivity V_{sen} and power sensitivity P_{sen} for the optimal stiffness case and they reach 84.4% and 71.3% of those from the theory, respectively.

Figure 8(*a*) plots the normalized experimental first mode shapes for the proof mass cantilever and PCM. The squares, circles, and triangles represent the experimental displacement data collected

Table 3 Performance comparison

	Proof mass cantilever		PCM		
	Theory	Experiment	Theory	Experiment	Units
First resonance frequency, f_{re}	5.22	5.28	5.02	5.13	Hz
Strain limit, S_{lim}	0.183%		0.183%		
Optimal load resistance, R_{opt}	22.0		22.9		MΩ
Theoretical maximum power $P_{max,theory}$ at S_{lim}	21.0		20.2		μW
Load resistance, R_l	5.31	5.25	5.36	5.25	MΩ
Tip displacement sensitivity, d_{sen}	0.185	0.175	0.0867	0.0812	m/g
Voltage sensitivity, V_{sen}	103	90.7	59.0	49.8	V/g
Power sensitivity, P_{sen}	2.03	1.57	0.662	0.472	mW/g^2
Maximum strain sensitivity, S_{sen}	3.37%	3.52%	1.05%	1.01%	1/g
Maximum voltage V_{max} at S_{lim}	5.62	4.72	10.3	9.06	V
Maximum power P_{max} at S_{lim}	6.02	4.24	20.2	15.6	μW
Mode shape efficiency, η	28.6%	20.2%	99.9%	77.4%	

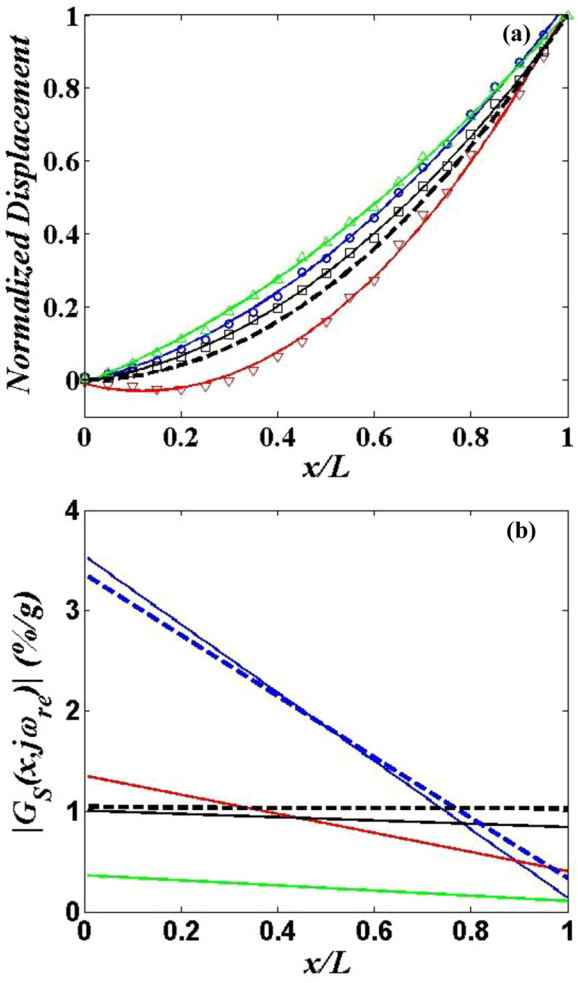

Fig. 8 (*a*) Normalized mode shapes and (*b*) maximum strain distributions for the proof mass cantilever theory (blue dashed line) and experiment (blue solid line with circles), PCM theory (black dashed line) and experiment (optimal stiffness: black solid line with squares, lower stiffness: red solid line with downward-pointing triangles, and higher stiffness: green solid line with upward-pointing triangles; see online figure for color)

along the piezoelectric beams and the lines are third-order polynomial fits. The theoretical first mode shape of the PCM energy harvester is parabolic, shown as the black dashed line in Fig. 8(*a*). As can be seen, the experimental PCM optimal stiffness mode shape (black solid line) is much closer to a parabola than the lower stiffness case (red solid line), higher stiffness case (green solid line), and the cantilever (blue solid line; see online figure for color), indicating that the optimal stiffness case has the highest mode shape efficiency. The spatial second derivative of the beam displacement is used to calculate the maximum strain based on Eq. (23) and normalized by base acceleration to obtain the maximum strain distribution shown in Fig. 8(*b*). Theoretical maximum strain distribution for the cantilever and PCM are also plotted using Eq. (24) and compare well with the experiment. For the PCM optimal stiffness case, the strain distribution is almost uniform, resulting in a high experimental efficiency of 77.4%. The strain in the proof mass cantilever, however, is maximum at the base and decreases linearly along the length, resulting in a relatively small efficiency of 20.2%.

6.3 Strain Limit and Fatigue Analysis. Inertial and electromechanical coupling, mechanical strain/fatigue, and electrical energy extraction limit the power generation of piezoelectric energy harvesters [30]. For harvesters having a mechanical quality factor greater than 5, mechanical fatigue and strain limitations dominate [31]. The energy harvesters in this paper have first mode damping ratios less than 5%, corresponding to quality factors larger than ten, so mechanical fatigue and strain concerns limit the power density. If the piezoelectric material exceeds its strain limit, micro cracks will occur, disconnecting active material and lowering the piezoelectric response. The design process should therefore evaluate the maximum strain and apply a design constraint to prevent mechanical failure.

In practice, the maximum strain must be limited to ensure an infinite fatigue life of the device. To allow for a reasonable safety margin for practical application, design uses a safety factor k to determine the practically safe tensile strength limit

$$\sigma_{lim} = \frac{\sigma_y}{k} \tag{40}$$

where σ_y is the yield strength of the piezoelectric material [30,32,33]. From Eq. (40), the resulting strain limit

$$S_{lim} = \frac{\sigma_{lim}}{E_p} = \frac{\sigma_y}{kE_p} \tag{41}$$

Substituting PVDF properties from Table 2 into Eq. (41), we obtain the strain limit S_{lim} of 0.183% for both devices with a safety factor of ten.

The tip displacement sensitivity d_{sen} and maximum strain sensitivity S_{sen} of the cantilever are over two and three times larger than those of the PCM, respectively, indicating that if these two devices are used under the same excitation, the piezoelectric material in the proof mass cantilever suffers from larger strain cycles and degrades and fails in less time. The PCM bridge structure can self-limit the response to large amplitude impacts, improving the

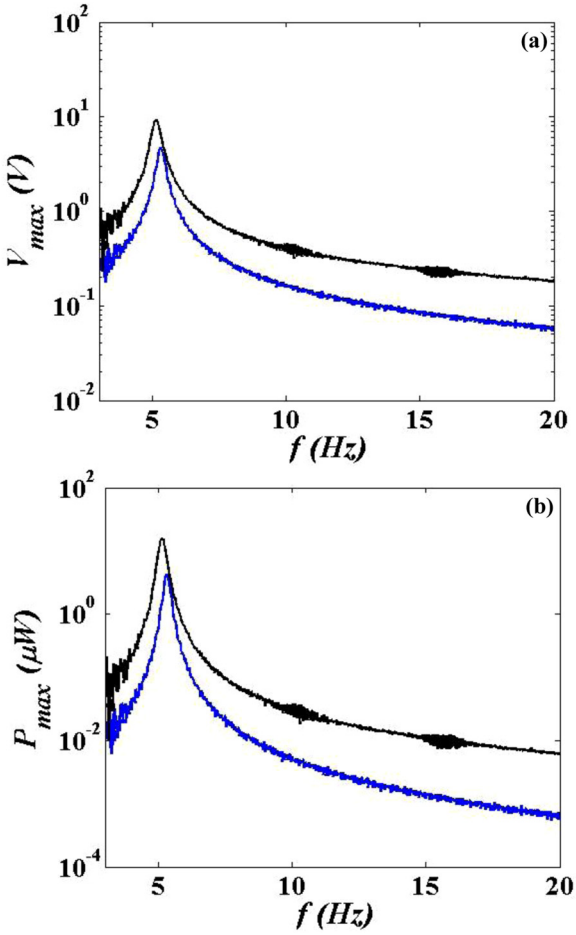

Fig. 9 Experimental (*a*) maximum voltage and (*b*) maximum power at the strain limit for the proof mass cantilever (blue solid line) and PCM (black solid line; see online figure for color)

robustness of the device. This advantage also results in the comparably smaller voltage sensitivity V_{sen} of the PCM. The same base excitation generates larger tip displacement and voltage output for the cantilever compared to the PCM. Figure 9 shows the maximum voltage and power that can be generated at the strain limit S_{lim} for both the cantilever and PCM. The PCM outperforms proof mass cantilever at the same strain limit, generating twice the voltage and four times the power of the proof mass cantilever at the resonance frequency (see Table 3).

Despite the lower voltage and power sensitivity of the PCM, it will produce more power than the proof mass cantilever in real applications, where the device must have a long fatigue life. For example, the authors have recently designed devices to be worn on a human wrist during running, jogging, and walking [8]. For these two designs, the tip displacement response to the running input (most aggressive) reaches but does not exceed the maximum allowed tip displacement corresponding to 0.1% strain. If the structure is too soft, the tip displacement will exceed the maximum allowed value, overstraining the PZT. If the structure is too stiff, then the device will not generate enough power during walking. The piezoelectric beams on the two devices have the same area but different geometries to satisfy this design criterion. Results show that the average power produced by the PCM is over six, five, and three times larger than that of the proof mass cantilever during running, jogging, and walking activities, respectively.

7 Conclusions

A PCM energy harvester is designed and fabricated to provide a resonance frequency of 5 Hz for energy harvesting from human movement. Careful stiffness tuning enforces a PCM quadratic boundary condition, making the first mode shape close to a parabola and efficient. The PCM generates twice the voltage and four times the power of a proof mass cantilever under the same strain limit. The PCM design also limits the beam displacement, reducing high stress that can degrade and reduce the life of the harvester. Future work will focus on the nonlinear modeling and high amplitude testing to explain this phenomenon.

Acknowledgment

This work was supported by the National Science Foundation ASSIST Nanosystems ERC under Award No. EEC-1160483.

References

[1] Anton, S. R., and Sodano, H. A., 2007, "A Review of Power Harvesting Using Piezoelectric Materials (2003–2006)," Smart Mater. Struct., **16**(3), pp. R1–R21.
[2] Khaligh, A., Zeng, P., and Zheng, C., 2009, "Kinetic Energy Harvesting Using Piezoelectric and Electromagnetic Technologies—State of the Art," IEEE Trans. Ind. Electron., **57**(3), pp. 850–860.
[3] Granstrom, J., Feenstra, J., Sodano, H. A., and Farinholt, K., 2007, "Energy Harvesting From a Backpack Instrumented With Piezoelectric Shoulder Straps," Smart Mater. Struct., **16**(5), pp. 1810–1820.
[4] Shenck, N. S., and Paradiso, J. A., 2001, "Energy Scavenging With Shoe-Mounted Piezoelectrics," IEEE Micro, **21**(3), pp. 30–42.
[5] Delnavaz, A., and Voix, J., 2014, "Flexible Piezoelectric Energy Harvesting From Jaw Movements," Smart Mater. Struct., **23**(10), p. 105020.
[6] Gorlatova, M., Sarik, J., Cong, M., Kymissis, I., and Zussmant, G., 2014, "Movers and Shakers: Kinetic Energy Harvesting for the Internet of Things," ACM SIGMETR. Perf. Eval. Rev., **42**(1), pp. 407–419.
[7] Ylli, K., Hoffmann, D., Willmann, A., Becker, P., Folkmer, B., and Manoli, Y., 2015, "Energy Harvesting From Human Motion: Exploiting Swing and Shock Excitations," Smart Mater. Struct., **24**(2), p. 025029.
[8] Ma, X., Yeo, H. G., Rahn, C. D., and Trolier-McKinstry, S., 2015, "Efficient and Sensitive Energy Harvesting Using Piezoelectric MEMS Compliant Mechanisms," ASME Paper No. DETC2015-47539.
[9] Shen, D., Park, J.-H., Ajitsaria, J., Choe, S.-Y., Wikle, H. C., III, and Kim, D.-J., 2008, "The Design, Fabrication and Evaluation of a MEMS PZT Cantilever With an Integrated Si Proof Mass for Vibration Energy Harvesting," J. Micromech. Microeng., **18**(5), p. 055017.
[10] Renaud, M., Fiorini, P., and van Hoof, C., 2007, "Optimization of a Piezoelectric Unimorph for Shock and Impact Energy Harvesting," Smart Mater. Struct., **16**(4), pp. 1125–1135.
[11] Erturk, A., and Inman, D. J., 2008, "A Distributed Parameter Electromechanical Model for Cantilevered Piezoelectric Energy Harvesters," ASME J. Vib. Acoust., **130**(4), p. 041002.
[12] Erturk, A., and Inman, D. J., 2009, "An Experimentally Validated Bimorph Cantilever Model for Piezoelectric Energy Harvesting From Base Excitations," Smart Mater. Struct., **18**(2), p. 025009.
[13] Ajitsaria, J., Choe, S. Y., Shen, D., and Kim, D. J., 2007, "Modeling and Analysis of a Bimorph Piezoelectric Cantilever Beam for Voltage Generation," Smart Mater. Struct., **16**(2), pp. 447–454.
[14] Xue, H., Hu, Y., and Wang, Q.-M., 2008, "Broadband Piezoelectric Energy Harvesting Devices Using Multiple Bimorphs With Different Operating Frequencies," IEEE Trans. Ultrason. Ferroelectr. Freq. Control, **55**(9), pp. 2104–2108.
[15] Aladwani, A., Aldraihem, O., and Baz, A., 2014, "A Distributed Parameter Cantilevered Piezoelectric Energy Harvester With a Dynamic Magnifier," Mech. Adv. Mater. Struct., **21**(7), pp. 566–578.
[16] Kim, S., Clark, W. W., and Wang, Q.-M., 2005, "Piezoelectric Energy Harvesting With a Clamped Circular Plate: Analysis," J. Intell. Mater. Syst. Struct., **16**(10), pp. 847–855.
[17] Kim, S., Clark, W. W., and Wang, Q.-M., 2005, "Piezoelectric Energy Harvesting With a Clamped Circular Plate: Experimental Study," J. Intell. Mater. Syst. Struct., **16**(10), pp. 855–863.
[18] Jung, S.-M., and Yun, K.-S., 2010, "Energy-Harvesting Device With Mechanical Frequency-Up Conversion Mechanism for Increased Power Efficiency and Wideband Operation," Appl. Phys. Lett., **96**(11), p. 111906.
[19] Galchev, T., Aktakka, E. E., and Najafi, K., 2012, "A Piezoelectric Parametric Frequency Increased Generator for Harvesting Low-Frequency Vibrations," J. Microelectromech. Syst., **21**(6), pp. 1311–1320.
[20] Pillatsch, P., Yeatman, E. M., and Holmes, A. S., 2013, "Magnetic Plucking of Piezoelectric Beams for Frequency Up-Converting Energy Harvesters," Smart Mater. Struct., **23**(2), p. 25009.
[21] Kulah, H., and Najaf, K., 2008, "Energy Scavenging From Low-Frequency Vibrations by Using Frequency Up-Conversion for Wireless Sensor Applications," IEEE Sens. J., **8**(3), pp. 261–268.
[22] Zorlu, O., Topal, E. T., and Kulah, H., 2011, "A Vibration-Based Electromagnetic Energy Harvester Using Mechanical Frequency Up-Conversion Method," IEEE Sens. J., **11**(3), pp. 481–488.
[23] Gu, L., and Livermore, C., 2011, "Impact-Driven, Frequency Up-Converting Coupled Vibration Energy Harvesting Device for Low Frequency Operation," Smart Mater. Struct., **20**(4), p. 045004.

[24] Liu, H., Lee, C., Kobayashi, T., Tay, C. J., and Quan, C., 2012, "Piezoelectric MEMS-Based Wideband Energy Harvesting Systems Using a Frequency-Up-Conversion Cantilever Stopper," Sens. Actuators A, **186**, pp. 242–248.
[25] Yoon, H.-S., Washington, G., and Danak, A., 2005, "Modeling, Optimization, and Design of Efficient Initially Curved Piezoceramic Unimorphs for Energy Harvesting Applications," J. Intell. Mater. Syst. Struct., **16**(10), pp. 877–888.
[26] Roundy, S., Leland, E. S., Baker, J., Carleton, E., Reilly, E., Lai, E., Otis, B., Rabaey, J. M., Wright, P. K., and Sundararajan, V., 2005, "Improving Power Output for Vibration-Based Energy Scavengers," IEEE Pervasive Comput., **4**(1), pp. 28–36.
[27] Lobontiu, N., 2002, *Compliant Mechanisms: Design of Flexure Hinges*, CRC Press, Boca Raton.
[28] Banks, H. T., and Inman, D. J., 1991, "On Damping Mechanisms in Beams," ASME J. Appl. Mech., **58**(3), pp. 716–723.
[29] Measurement Specialties, I., 2012, *Piezo Film Sensors Technical Manual*, Sensor Products Division, Measurement Specialties, Norristown, PA.
[30] Dompierre, A., Vengallatore, S., and Frechette, L. G., 2011, "Theoretical and Practical Limits of Power Density for Piezoelectric Vibration Energy Harvesters," 11th International Workshop on Micro and Nanotechnology for Power Generation and Energy Conversion Applications (PowerMEMS 2011), Seoul, Korea, Nov. 15–18, pp. 249–252.
[31] Dubus, B., Debus, J. C., Decarpigny, J. N., and Boucher, D., 1991, "Analysis of Mechanical Limitations of High Power Piezoelectric Transducers Using Finite Element Modelling," Ultrasonics, **29**(3), pp. 201–207.
[32] Measurement Specialties, I., 2010, *Power Generation Using Piezo Film*, Measurement Specialties, Aliso Viejo, CA.
[33] Marines, I., Bin, X., and Bathias, C., 2003, "An Understanding of Very High Cycle Fatigue of Metals," Int. J. Fatigue, **25**(9–11), pp. 1101–1107.